minerals

MDPI

Article

Impulsive Supply of Volatile-Rich Magmas in the Shallow Plumbing System of Mt. Etna Volcano

Cristina Perinelli [1,*], Silvio Mollo [1,2], Mario Gaeta [1], Serena Pia De Cristofaro [3], Danilo Mauro Palladino [1] and Piergiorgio Scarlato [2]

1 Dipartimento di Scienze della Terra, Sapienza-Università di Roma, P.le Aldo Moro 5, 00185 Roma, Italy; silvio.mollo@uniroma1.it (S.M.); mario.gaeta@uniroma1.it (M.G.); danilo.palladino@uniroma1.it (D.M.P.)
2 Istituto Nazionale di Geofisica e Vulcanologia, Via di Vigna Murata 605, 00143 Roma, Italy; piergiorgio.scarlato@ingv.it
3 Dipartimento di Scienze della Terra, Università degli Studi di Torino, Via Valperga Caluso 35, 10125 Torino, Italy; serenapia.decristofaro@unito.it
* Correspondence: cristina.perinelli@uniroma1.it; Tel.: +39-06-49914916

Received: 18 September 2018; Accepted: 22 October 2018; Published: 25 October 2018

Abstract: Magma dynamics at Mt. Etna volcano are frequently recognized as the result of complex crystallization regimes that, at shallow crustal levels, unexpectedly change from H_2O-undersaturated to H_2O-saturated conditions, due to the impulsive and irregular arrival of volatile-rich magmas from mantle depths. On this basis, we have performed hydrous crystallization experiments for a quantitative understanding of the role of H_2O in the differentiation of deep-seated trachybasaltic magmas at the key pressure of the Moho transition zone. For H_2O = 2.1–3.2 wt %, the original trachybasaltic composition shifts towards phonotephritic magmas never erupted during the entire volcanic activity of Mt. Etna. Conversely, for H_2O = 3.8–8.2 wt %, the obtained trachybasalts and basaltic trachyandesites reproduce most of the pre-historic and historic eruptions. The comparison with previous low pressure experimental data and natural compositions from Mt. Etna provides explanation for (1) the abundant release of H_2O throughout the plumbing system of the volcano during impulsive ascent of deep-seated magmas; (2) the upward acceleration of magmas feeding gas-dominated, sustained explosive eruptions; (3) the physicochemical changes of gas-fluxed magmas ponding at shallow crustal levels; and (4) the huge gas emissions measured at the summit craters and flank vents which result in a persistent volcanic gas plume.

Keywords: Mt. Etna; high-pressure experiments; magma ascent; H_2O release

1. Introduction

The plumbing system of Mt. Etna volcano (Sicily, Italy) has a multifaceted geometry, variable in space and time and consisting of storage zones at different depths, where more or less primitive magmas containing variable H_2O contents undergo degassing, fractional crystallization and mixing processes (cf. [1]). For example, the explosive activity of the volcano is ascribed to the impulsive upward migration of gas-rich magmas and/or fluxes of abundant volatiles from the depths [2–4]. Evidence of pulsating volatile flushing is also provided by the great volume of gases released from the summit craters and flanks of the volcano that clashes with the relatively small amount of erupted products [5]. The release of volatiles has drastic effects on the rheology of Etnean magmas and, consequently, the internal dynamics of the volcano [6]. Moreover, the large quantities of gas released may change the geochemical and isotopic compositions of near-liquidus lavas erupted at the vents and flowing onto the surface [7].

In this scenario, the vertically developed plumbing system represents a pathway for volatiles migration as supercritical fluids [4,8,9]. The impulse migration of volatiles through magmas stored beneath (or within) the volcanic edifice changes the physicochemical state of the system from H_2O-undersaturated to H_2O-saturated, with implications for mineral and melt compositions, degree of crystallization, magma ascent velocity and style of eruption [1,3,4,8,10–13].

Relevant insights into the highly variable volatile concentrations of magmas (H_2O = 0.5–3.5 wt % and CO_2 = 0.02–0.25 wt %) have been provided by data on melt inclusions entrapped at both shallow and moderate pressures (25–400 MPa) [14]. Within this pressure range, the differentiation process of Etnean liquids upon the effect of variable H_2O concentrations have been explored through hydrous crystallization experiments [13,15–17]. However, few data are available in the literature at the key pressure of the Moho transition zone (~800 MPa or ~24 km b.s.l.; [18]) at which the solubility of H_2O may be very high (>10 wt %; [19,20] and references therein), thus remarkably influencing the early crystallization of gas-rich trachybasaltic magmas erupted at Mt. Etna [12,21].

In this study, we present hydrous crystallization experiments conducted at 800 MPa, 1020–1200 °C, 2.1–10 wt % H_2O, and NNO buffer with the aim of better understanding the role of H_2O in the differentiation of deep-seated trachybasaltic magmas. Considering the crystallization temperatures at the Moho depth recorded by clinopyroxene phenocrysts from lava fountains and lava flows, the results of our experiments show that the irregular arrival of deep-seated, volatile-rich magmas into the uppermost portions of the plumbing system may release a huge amount of H_2O with remarkable implications for the dynamics of H_2O-undersaturated magmas ponding at shallow crustal levels.

2. Starting Materials and Methods

The starting materials used in this study are two trachybasalts (i.e., HE and ME hawaiitic products) from Mt. Etna showing virtually identical compositions: on anhydrous basis, HE and ME have 47.78 and 48.27 wt % SiO_2, and 5.87 and 5.79 wt % Na_2O + K_2O, respectively (Table 1). HE is a lava flow erupted from the western flank of the Valle del Bove during the 1991–1993 effusive activity [22]. ME is a lava flow erupted from the South-East Crater during the 2011–2013 paroxysmal activity comprising both Strombolian explosions and lava effusions [23,24]. These two compositions are, indeed, the most representative of the recent activity at Mt. Etna volcano.

Table 1. Composition of HE and ME starting materials. SD is the standard deviation.

#Oxide	HE	SD (5)	ME	SD (5)
Experimental melt compositions				
SiO_2	47.78	0.39	48.27	0.43
TiO_2	1.72	0.02	1.69	0.03
Al_2O_3	17.10	0.19	17.32	0.16
FeO_{tot}	10.18	0.12	11.07	0.11
MnO	0.17	0.01	0.17	0.03
MgO	5.55	0.07	4.94	0.09
CaO	10.40	0.12	9.94	0.10
Na_2O	3.84	0.05	3.73	0.07
K_2O	2.03	0.03	2.06	0.05
P_2O_5	0.55	0.01	0.57	0.03
Tot	99.32		99.76	

Notes: FeO_{tot} is the total iron given as FeO.

Both experiments and analyses were conducted at the Department of Earth Sciences, Sapienza-University of Rome, Italy. The starting glass was produced by melting the powdered sample at 1350 °C and atmospheric pressure for 1 h. Some glass chips were then analyzed by scanning electron microscopy, and no crystalline phases were detected. Phase equilibrium crystallization experiments were performed at 800 MPa in a half-inch, end-loaded piston cylinder apparatus. The starting material, composed of the powdered glass and deionized H_2O, was loaded into a $Au_{75}Pd_{25}$ capsule. Variable

amounts of H_2O were added to the charges in order to obtain melt-H_2O concentrations in the range between 2.1 and 10 wt % (Table 2), as determined by the "difference from 100" method (i.e., based on the difference to 100% of the total obtained by microprobe analyses of glasses, with accuracy of ~0.5 wt % H_2O; [25].

According to H_2O solubility data ([19] see discussion below) and the absence of gas bubbles into the quenched charges, the experiments were H_2O-undersaturated, thus reproducing the crystallization conditions observed for Etnean magmas residing at depth [26]. The assembly consisted of fluorite-graphite-magnesia. The charge was heated directly to the target temperature (i.e., between 1020 and 1200 °C) that was kept constant for 8 h (Table 2). The temperature was controlled by a factory calibrated thermocouple ($W_{95}Re_5$-$W_{74}Re_{26}$; type D) with accuracy of ± 3 °C. The experiment was quenched through a cooling rate of approximately 150 °C/s and then the run product was mounted in an epoxy disk to expose a polished surface.

All the runs were self-buffered; we attempted to estimate fO_2 through the equation of [27] using the liquid Fe^{3+}/Fe_{tot} mole ratios from olivine-melt Fe-Mg exchange calculated according to [28]. This procedure yielded fO_2 values of −0.3 to +0.7 NNO, in agreement with those estimated for similar furnace assemblages [29,30].

The chemical analyses were performed at the CNR-Istituto di Geologia Ambientale e Geoingegneria (Rome, Italy) using a Cameca SX50 electron microprobe (CAMECA, Gennevilliers, France) equipped with five wavelength-dispersive spectrometers using 15 kV accelerating voltage, 15 nA beam current for minerals and 2 nA for glass to obviate the alkali loss during the analyses, particularly for hydrous glasses. Moreover, sodium and potassium were analyzed first to prevent alkali migration effects. The beam diameter was of 10 µm, and the counting time was 20 s. The following standards were used: wollastonite (Si and Ca), corundum (Al), diopside (Mg), andradite (Fe), rutile (Ti), orthoclase (K), jadeite (Na), apatite (P) and metal (Mn).

Table 2. Experimental conditions, mass balance calculations, and tests for equilibrium crystallization conditions.

Run	T	t	H_2O	Gl	Cpx	Plg	Timt	Ol	Σr^2	${}^{cpx\text{-}melt}Kd_{Fe\text{-}Mg}$	ΔDiHd	${}^{plg\text{-}melt}Kd_{Ab\text{-}An}$	${}^{ol\text{-}melt}Kd_{Fe\text{-}Mg}$
(#)	(°C)	(h)	(wt %)	(wt %–vol %)						(Putirka et al., 2008)	(Mollo et al., 2013b)	(Putirka et al., 2008)	Roeder and Emslie (1970)
HE-1	1200	8	2.7	100–100	-	-	-	-	0.01	-	-	-	-
HE-2	1125	8	2.1	59–57	23–24	15–16	2–2	1–1	0.25	0.26	0.03	0.14	0.42
HE-3	1050	8	8.2	85–87	9–8	-	6–5	-	0.19	0.27	0.05	-	-
HE-4	1020	8	10	100–100	-	-	-	-	0.01	-	-	-	-
ME-1	1175	8	3.2	87–88	6–5	6–6	1–1	-	0.32	0.27	0.02	0.21	-
ME-2	1150	8	2.3	64–67	11–10	18–16	4–4	3–3	0.19	0.27	0.04	0.18	0.35
ME-3	1150	8	6.2	100–100	-	-	-	-	0.01	-	-	-	-
ME-4	1125	8	2.4	69–73	13–12	15–14	1–1	2–2	0.21	0.27	0.08	0.14	0.54
ME-5	1090	8	4.1	48–53	17–15	26–24	5–4	4–4	0.31	0.27	0.04	0.17	0.26
ME-6	1070	8	3.8	48–53	18–16	28–26	1–1	5–4	0.26	0.27	0.01	0.15	0.49
ME-7	1065	8	5.0	56–60	11–10	24–22	6–5	3–3	0.24	0.27	0.07	0.14	0.55

3. Results

3.1. Phase Relations

Modal phase proportions (wt %) were derived by mass balance calculations [31], yielding acceptable residual sum of squares ($\Sigma r^2 < 0.32$; see Table 2). For a better comparison of these estimates with vol % data from lava flows, the volume proportions were recalculated using average densities of olivine (3.3 g/cm^3) clinopyroxene (3.4 g/cm^3), plagioclase (2.6 g/cm^3), titanomagnetite (5.1 g/cm^3) and melt (2.6–2.7 g/cm^3 from the model of [32]). According to [17], both wt % and vol % estimates provided almost identical values (Table 2).

Figure 1 shows that the phase assemblage is characterized by the ubiquitous occurrence of clinopyroxene and titanomagnetite at near-liquidus conditions, followed by the crystallization of plagioclase and olivine at lower temperatures and/or H_2O contents. In highly crystallized charges, plagioclase is the most abundant mineral phase but its stability field progressively decreases with increasing H_2O. The crystallization of clinopyroxene and plagioclase increases by 50 vol % with decreasing temperature (Table 2). In particular, the plagioclase/clinopyroxene ratio is 0.7–1.2 at $T \geq 1125$ °C, but abruptly increases to 1.5–2.2 at $T \leq 1090$ °C due to the predominant crystallization of plagioclase (Table 2). It is interesting to note that olivine crystallization occurs only at $T \leq 1150$ °C and is subordinated to that of other mineral phases.

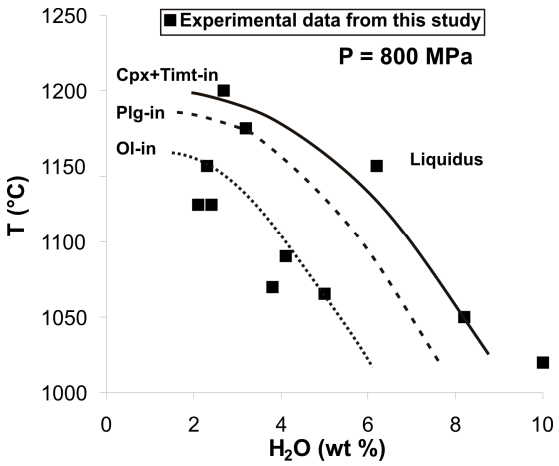

Figure 1. Temperature vs. H_2O diagram showing the stability of mineral phases in our experimental charges. As the temperature decreases, the near-liquidus surface is gained by increasing amounts of H_2O that lower the degree of crystallization and buffer the melt composition to trachybasalt. Cpx, clinopyroxene. Timt, titanomagnetite. Plg, plagioclase. Ol, olivine.

3.2. Phase Compositions

Major element concentrations of both experimental glasses and minerals are reported in Table 3. In the total alkali versus silica diagram (Figure 2), the original trachybasaltic melt obtained at H_2O = 2.1–3.2 wt % evolves towards basaltic trachyandesitic and phonotephritic compositions, as well as the Mg-number (i.e., Mg# = atomic Mg/(Mg + Fe^{2+}) × 100) decreases from $Mg\#_{42}$ to $Mg\#_{37}$. At H_2O = 3.8–8.2 wt %, the starting melt differentiates from basaltic trachyandesite to trachyandesite to tephriphonolite with $Mg\#_{33–43}$. The residual melts show a significant increase of SiO_2 content (from 48.89 to 53.39 wt %) associated with a narrow increase of alkali (from 6.49 to 9.57 wt %) that, in turn, is weakly observed at H_2O = 2.1–3.2 wt % (Figure 2).

Table 3. Experimental compositions of residual melts, clinopyroxenes, plagioclases, titanomagnetites, and olivines. SD is the standard deviation.

#	HE-2	SD(4)	HE-3	SD(4)	ME-1	SD(4)	ME-2	SD(4)	ME-4	SD(4)	ME-5	SD(4)	ME-6	SD(4)	ME-7	SD(4)
Experimental melt compositions																
SiO_2	50.96	0.40	51.71	0.38	49.88	0.45	50.86	0.43	50.69	0.45	53.51	0.42	53.21	0.45	53.49	0.41
TiO_2	2.00	0.02	1.49	0.02	1.75	0.02	2.00	0.03	1.92	0.03	1.89	0.02	1.86	0.03	2.05	0.02
Al_2O_3	18.16	0.20	19.75	0.20	17.63	0.15	17.32	0.12	17.87	0.16	18.61	0.20	18.78	0.13	15.97	0.17
FeO	8.35	0.10	6.08	0.06	9.59	0.14	9.50	0.09	9.57	0.10	7.40	0.07	7.08	0.07	8.35	0.12
MnO	0.16	0.02	0.20	0.03	0.14	0.00	0.20	0.02	0.22	0.01	0.21	0.03	0.24	0.01	0.20	0.01
MgO	3.29	0.06	4.23	0.07	4.64	0.09	3.79	0.04	3.91	0.05	2.45	0.05	2.80	0.03	4.21	0.08
CaO	7.03	0.06	9.65	0.11	9.39	0.07	7.41	0.07	7.05	0.07	5.76	0.04	5.60	0.05	7.36	0.07
Na_2O	5.76	0.10	4.34	0.05	4.26	0.04	5.13	0.06	4.87	0.06	4.99	0.06	5.38	0.06	4.64	0.08
K_2O	3.31	0.07	2.23	0.03	2.22	0.03	3.12	0.05	3.20	0.08	4.32	0.06	4.16	0.06	3.02	0.07
P_2O_5	0.98	0.02	0.33	0.02	0.49	0.01	0.67	0.03	0.70	0.03	0.86	0.04	0.89	0.02	0.72	0.03
Total	97.91		91.82		96.82		97.68		97.60		95.90		96.19		95.02	
#	**HE-2**	**SD(3)**	**HE-3**	**SD(3)**	**ME-1**	**SD(3)**	**ME-2**	**SD(3)**	**ME-4**	**SD(3)**	**ME-5**	**SD(3)**	**ME-6**	**SD(3)**	**ME-7**	**SD(3)**
Experimental clinopyroxene compositions																
SiO_2	47.86	0.39	48.95	0.40	48.95	0.40	48.56	0.39	49.56	0.40	49.35	0.40	49.29	0.40	48.73	0.39
TiO_2	1.85	0.02	0.88	0.01	1.51	0.02	1.54	0.02	1.36	0.02	1.55	0.02	1.26	0.02	1.52	0.02
Al_2O_3	6.22	0.12	5.34	0.10	4.98	0.09	5.34	0.10	4.56	0.09	4.52	0.09	4.63	0.09	4.99	0.09
FeO	8.59	0.10	6.68	0.08	8.32	0.10	8.55	0.10	8.24	0.10	8.66	0.10	7.67	0.09	8.47	0.10
MnO	0.19	0.02	0.16	0.01	0.19	0.02	0.16	0.01	0.21	0.02	0.38	0.03	0.20	0.02	0.20	0.02
MgO	12.25	0.15	14.86	0.18	12.79	0.15	12.57	0.15	13.15	0.16	12.64	0.15	13.49	0.16	12.74	0.15
CaO	22.40	0.27	22.46	0.27	22.77	0.27	22.54	0.27	21.79	0.26	22.13	0.27	22.89	0.27	22.68	0.27
Na_2O	0.42	0.03	0.60	0.04	0.47	0.03	0.48	0.03	0.53	0.03	0.58	0.03	0.73	0.04	0.44	0.03
Total	99.77		99.93		99.99		99.74		99.39		99.81		100.17		99.76	
Cations on the basis of 6 oxygens																
Si	1.789		1.796		1.822		1.813		1.853		1.843		1.631		1.819	
Ti	0.211		0.204		0.178		0.187		0.147		0.157		0.169		0.181	
Al^{IV}	0.063		0.027		0.040		0.048		0.053		0.042		0.032		0.038	
Al^{VI}	0.052		0.024		0.042		0.043		0.038		0.043		0.035		0.043	
Fe^{3+}	0.076		0.172		0.089		0.089		0.056		0.072		0.121		0.092	
Fe^{2+}	0.192		0.033		0.170		0.178		0.201		0.199		0.115		0.173	

Table 3. *Cont.*

Cations on the basis of 6 oxygens														
Mn	0.682		0.813		0.710		0.699		0.733		0.703		0.738	0.709
Mg	0.006		0.005		0.006		0.005		0.007		0.012		0.006	0.006
Ca	0.897		0.883		0.908		0.902		0.873		0.886		0.900	0.907
Na	0.030		0.042		0.034		0.035		0.038		0.042		0.052	0.032
Di	0.58		0.67		0.62		0.60		0.60		0.60		0.65	0.62
Hd	0.16		0.03		0.15		0.15		0.16		0.17		0.10	0.15
En	0.05		0.07		0.04		0.05		0.07		0.05		0.04	0.05
Fs	0.02		0.00		0.01		0.01		0.02		0.01		0.01	0.01
Jd	0.03		0.03		0.04		0.04		0.04		0.04		0.03	0.03
CaTs	0.07		0.08		0.05		0.06		0.04		0.04		0.05	0.05
CaFeTs	0.04		0.09		0.04		0.04		0.03		0.04		0.06	0.05
#	**HE-2**	**SD(3)**	**ME-1**	**SD(3)**	**ME-2**	**SD(3)**	**ME-4**	**SD(3)**	**ME-5**	**SD(3)**	**ME-6**	**SD(3)**	**ME-7**	**SD(3)**
Experimental plagioclase compositions														
SiO_2	46.72	0.38	48.91	0.40	52.40	0.42	52.10	0.42	52.30	0.42	50.21	0.41	51.27	0.42
TiO_2	0.12	0.01	0.05	0.00	0.09	0.01	0.08	0.01	0.10	0.01	0.07	0.01	0.11	0.01
Al_2O_3	32.31	0.36	31.35	0.34	28.99	0.32	29.92	0.33	28.75	0.32	30.42	0.33	29.99	0.33
FeO	0.96	0.04	0.80	0.03	0.81	0.03	0.85	0.04	1.10	0.05	0.98	0.04	0.94	0.04
MgO	0.10	0.01	0.09	0.01	0.09	0.01	0.09	0.01	0.16	0.01	0.09	0.01	0.10	0.01
CaO	16.61	0.20	15.46	0.19	13.01	0.16	13.62	0.16	13.07	0.16	14.08	0.17	13.74	0.16
Na_2O	2.98	0.13	2.67	0.11	3.99	0.17	3.51	0.15	3.81	0.16	3.81	0.16	3.43	0.14
K_2O	0.16	0.01	0.21	0.01	0.44	0.03	0.34	0.02	0.45	0.03	0.31	0.02	0.38	0.02
Total	99.96		99.53		99.82		100.51		99.74		99.96		99.97	
Cations on the basis of 8 oxygens														
Si	2.164		2.253		2.391		2.361		2.390		2.301		2.341	
Al	1.764		1.702		1.560		1.598		1.549		1.644		1.614	
Fe	0.037		0.031		0.031		0.032		0.042		0.037		0.036	
Mg	0.001		0.001		0.001		0.001		0.001		0.001		0.001	
Ca	0.824		0.763		0.636		0.661		0.640		0.692		0.672	
Na	0.268		0.238		0.353		0.308		0.338		0.339		0.304	
K	0.010		0.012		0.025		0.019		0.026		0.018		0.022	
An	75		75		63		67		64		66		67	
Ab	24		24		35		31		34		32		30	
Or	1		1		2		2		3		2		2	

Table 3. *Cont.*

#	HE-2	SD(3)	HE-3	SD(3)	ME-5	SD(3)
Experimental titanomagnetite compositions						
TiO_2	10.15	0.11	10.14	0.12	10.03	0.12
Al_2O_3	6.32	0.32	5.28	0.26	5.43	0.27
FeO	73.01	0.66	71.45	0.79	74.61	0.60
MnO	0.38	0.05	0.62	0.07	0.42	0.05
MgO	4.19	0.25	1.53	0.09	1.89	0.11
Total	94.05		89.01		92.38	
Cations on the basis of 3 oxygens						
Ti	0.275		0.297		0.283	
Al	0.269		0.243		0.240	
Fe3+	0.000		0.000		0.000	
Fe2+	2.203		2.330		2.340	
Mn	0.012		0.020		0.013	
Mg	0.225		0.089		0.106	
Usp	32		37		34	

#	HE-2	SD(3)	ME-2	SD(3)	ME-4	SD(3)	ME-5	SD(3)	ME-6	SD(3)	ME-7	SD(3)
Experimental olivine compositions												
SiO_2	37.28	0.30	38.34	0.31	38.57	0.31	38.07	0.31	37.28	0.30	38.07	0.31
FeO	30.13	0.36	22.81	0.27	24.79	0.30	23.33	0.28	30.13	0.36	23.33	0.28
MnO	0.74	0.04	0.66	0.03	0.64	0.03	0.59	0.03	0.74	0.04	0.59	0.03
MgO	31.08	0.34	36.57	0.40	35.28	0.39	36.47	0.40	31.08	0.34	36.47	0.40
CaO	0.43	0.03	0.44	0.04	0.44	0.02	0.39	0.03	0.43	0.02	0.39	0.03
Tot	99.66		98.82		99.72		98.85		99.66		98.85	
Cations on the basis of 4 oxygens												
Si	1.013		1.014		1.018		1.009		1.013		1.009	
Fe	0.685		0.504		0.547		0.517		0.685		0.517	
Mn	0.017		0.015		0.014		0.013		0.017		0.013	
Mg	1.259		1.441		1.389		1.441		1.259		1.441	
Ca	0.013		0.012		0.012		0.011		0.013		0.011	
Fo	65		74		72		74		65		74	

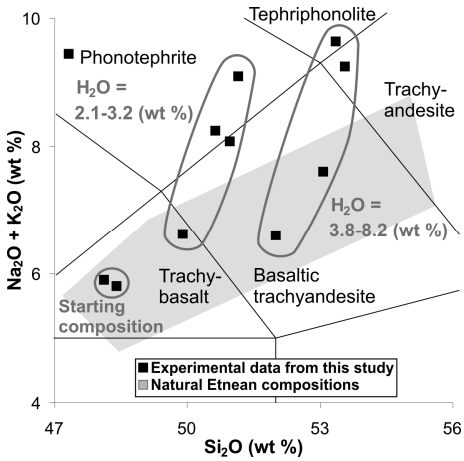

Figure 2. Total alkali vs. silica diagram showing the composition of residual melts from our experiments. Two distinct trends are depicted as a function of the H_2O content. For H_2O = 2.1–3.2 wt %, the original trachybasaltic liquid evolves towards basaltic trachyandesitic and phonotephritic compositions. For H_2O = 3.8–8.2 wt %, the starting melt differentiates to basaltic trachyandesitic to trachyandesitic to tephriphonolitic compositions.

The amount of diopside (Di) and hedenbergite (Hd) in clinopyroxene generally decreases with increasing temperature and H_2O (Table 3). At H_2O = 2.1–3.2 wt %, the ferri-calcium Tschermak molecule (CaFeTs) slightly decreases with decreasing temperature (Figure 3a). Conversely, at H_2O = 3.8–8.2 wt %, both Al^{iv} and Fe^{3+} are preferentially incorporated into clinopyroxene crystal lattice, leading to higher CaFeTs contents [33].

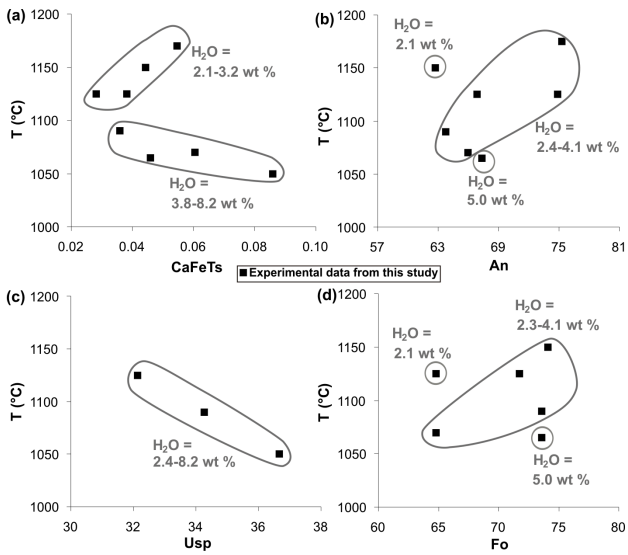

Figure 3. Mineral compositional variations as a function of temperature and melt-H_2O content. At H_2O = 2.1–3.2 wt %, the ferri-calcium Tschermak molecule (CaFeTs) slightly decreases with decreasing temperature, whereas at H_2O = 3.8–8.2 wt %, both Al^{iv} and Fe^{3+} are preferentially incorporated into clinopyroxene crystal lattice, leading to higher CaFeTs contents (**a**). The anorthite (An) molecule in plagioclase generally decreases with decreasing temperature with the exception of compositions derived upon the effect of H_2O = 2.1 and 5 wt % (**b**). The ulvospinel (Usp) content in titanomagnetite progressively increases along an almost linear trend resulting from the combined effect of both temperature and H_2O (**c**). At H_2O = 2.3–3.8 wt %, the amount of forsterite (Fo) in olivine decreases with decreasing temperature, whereas scattered Fo values are observed at H_2O = 2.1 and 5 wt % (**d**).

Overall, the anorthite (An) molecule in plagioclase shows a rough decrease (from An_{75} to An_{63}) with decreasing temperature (Figure 3b). However, An in plagioclase is also influenced by the initial H_2O content, according to the dependence of CaO-NaO exchange on hydroxyl groups dissolved in the melt [34].

The ulvospinel (Usp) content in titanomagnetite progressively increases along an almost linear trend resulting from the combined effect of both temperature and H_2O (Figure 3c). This compositional change is also associated with lower Al and Mg concentrations into the titanomagnetite crystal lattice, due to their preferential incorporation in clinopyroxene and plagioclase (Table 3).

At H_2O = 2.3–3.8 wt %, the amount of forsterite (Fo) in olivine decreases from 74 to 65 with decreasing temperature, whereas scattered Fo values are observed at the H_2O = 2.1 and 5 (Figure 3d). As documented for plagioclase, hydroxyl groups dissolved in the melt preferentially complex with Mg^{2+} rather than Fe^{2+}, thus reducing the activity of MgO relative to FeO in olivine, and *viceversa* [34].

3.3. Achievement of Equilibrium

In order to test the achievement of equilibrium crystallization in the experimental charges, different textural and compositional features have been considered: (1) the euhedral shape of crystals, (2) the homogeneous distribution of mineral phases in the glass, (3) the lack of quench crystals, (4) the smooth variation of phase compositions with experimental conditions, (5) the small sum of residuals (generally $\leq$0.5; Table 2) from mass-balance calculations, and (6) crystal-melt exchange coefficients (Kd) for clinopyroxene and plagioclase comparable to those from previous equilibrium studies. Concerning the clinopyroxene phase, we have used the temperature-sensitive ${}^{cpx\text{-}melt}Kd_{Fe\text{-}Mg}$ model derived by Putirka [35] and based on deviations in observed and calculated Fe-Mg cation partitioning between crystals and coexisting melts. ${}^{cpx\text{-}melt}Kd_{Fe\text{-}Mg}$ values of clinopyroxene-melt pairs from this study, calculated with the total Fe as Fe^{2+} according to Putirka et al. [36], vary between 0.26 and 0.27 (Table 2), in agreement with the equilibrium range of 0.27 $\pm$ 0.03 reported in literature (e.g., [36]). As a further test for clinopyroxene, we have also adopted the model of Mollo et al. [37], calibrated through the difference between diopside + hedenbergite components (ΔDiHd) predicted for clinopyroxene via regression analysis of clinopyroxene-melt pairs in equilibrium conditions, and those measured in the analyzed crystals (Table 2). ΔDiHd values derived for our experimental compositions are remarkably low (0.03–0.08) and close to zero, as expected for thermodynamically equilibrated phases (e.g., [38]).

The equilibrium crystallization of plagioclase has been tested through the Ab-An (albite-anorthite) exchange reaction proposed by Putirka [35]. According to this model, the equilibrium constant is constrained within two temperature-dependent intervals of ${}^{plg\text{-}melt}Kd_{Ab\text{-}An}$ = 0.10 $\pm$ 0.05 at T < 1050 °C and ${}^{plg\text{-}melt}Kd_{Ab\text{-}An}$ = 0.25 $\pm$ 0.11 at T > 1050 °C. Our estimates show that ${}^{plg\text{-}melt}Kd_{Ab\text{-}An}$ yields values between 0.15 and 0.21, suggesting equilibrium crystallization for experimental plagioclase crystals formed at T > 1050 °C.

4. Discussion

4.1. H_2O-Undersaturated Versus H_2O-Saturated Crystallization Regimes

Previous experiments conducted at 200–400 MPa on Etnean magmas have demonstrated that olivine does not crystallize under H_2O-undersaturated conditions [12,17,39], whereas at $P_{H2O} = P_{total}$ its stability field expands at the expense of other minerals, and olivine appears as liquidus phase [16]. A similar result has been also documented by the experimental study of Di Carlo et al. [40] for a K-basalt from Stromboli, where clinopyroxene dominates the phase assemblage at 400 and 300 MPa. Clinopyroxene and olivine co-saturate the melt at 200 MPa and olivine becomes the liquidus phase at 100 MPa and H_2O > 3.5 wt % [40]. Our experiments confirm that olivine is a late crystallizing phase from H_2O-undersaturated magmas equilibrated at high pressure. This agrees with the petrological observation of Tanguy et al. [41] that clinopyroxene oversteps olivine crystallization at the Moho depth (28 km, ~800 MPa; [18]), for most of the trachybasaltic lava flows erupted at Mt. Etna. Moreover,

thermobarometric estimates demonstrate that the initial stages of crystallization of Etnean trachybasalts take place near the Moho boundary [21], pointing to a deep feeder level of the plumbing system. We are aware of the critical role of CO_2 on the activity of H_2O in the melt and degassing/crystallization processes at Mt. Etna volcano, especially at high pressure, where the solubility of CO_2 may be significant (e.g., up to ~0.7 wt % at 800 MPa; [19]). However, previous experiments on Etnean trachybasalts show that phase relations and compositions are weakly affected by CO_2 concentration in the melt, successfully reproducing the textures and compositions of natural products under CO_2-absent experimental conditions. For example, Vetere et al. [17] have performed experiments on Etnean trachybasalts equilibrated at 400 MPa, 1100–1150 °C and NNO + 3.7 buffering conditions, as well as in presence of volatile components of 1–3 wt % H_2O and 0–0.3 wt % CO_2. Results from these experiments indicate that the role of CO_2 in controlling the final composition of magmas is negligible with respect to that played by T and H_2O at degrees of crystal fractionation in the range of 6–40 wt %. More specifically, in terms of major and rare earth elements, the Etnean compositions are well reproduced in laboratory irrespective of the C–O–H species in the melt phase. Logically, an increasing concentration of CO_2 in the melt reduces the solubility of H_2O, thus modulating the degree of crystal fractionation, as it is obtained by lowering the amount of H_2O added in the experimental charge.

In Figure 4, the compositions of pre-historic, 1963–1995, and 2001–2006 lava flows at Mt. Etna are compared with those experimentally derived at high (P = 800 MPa), moderate (P = 200–400 MPa) and low (P = 27–120 MPa) pressures (Table S1, Supplementary Materials). In H_2O-undersaturated experiments conducted at both high and moderate pressures, plagioclase crystallization is favored at low H_2O content, leading to a relatively high plagioclase/clinopyroxene ratio (Plg/Cpx = 0.7–2.2). As a consequence, the CaO/K_2O ratio in the melt decreases significantly at the early stage of crystallization, reproducing the bulk rock compositions of 2001–2006 eruptions, as well as part of the evolutionary trend of the less differentiated historic eruptions. In contrast, the high H_2O content in the low pressure experiments suppresses the crystallization of plagioclase along most of the magma differentiation path. Plagioclase starts to crystallize at low temperature (1075 °C) and the plagioclase/clinopyroxene ratio remains relatively low (Plg/Cpx = 0.3–0.9). Thus, the experimental melts exhibit high CaO/K_2O ratios that capture the bulk rock compositions of 1763–1995 eruptions.

According to Figure 4, it is apparent that the differentiation of Etnean magmas is controlled by the stability of plagioclase that, in turn, depends on the amount of H_2O dissolved in the melt. At very shallow crustal levels, the core-to-rim compositional variation of plagioclase phenocrysts is driven by the exsolution of ~3 wt % H_2O during magma decompression from 85 to 5 MPa [12]. Conversely, at P > 100 MPa, disequilibrium textures of plagioclase testify to mixing induced by recharge of volatile-rich magmas or injection by volatile flushing into the system [9,24]. This applies especially to the onset of lava fountain eruptions that are triggered by the irregular arrival of primitive, volatile-rich magma batches that mixed with more evolved, H_2O-undersaturated trachybasalts residing in the upper conduit region of the volcano [1,23].

In order to explain the most differentiated trachyandesitic lavas erupted during the pre-historic activity of Mt. Etna, we have modelled the evolution of the HE trachybasalt using the MELTS algorithm of Ghiorso and Sack [42] assuming a fractional crystallization process. The best fitting differentiation path is obtained at 1040–1160 °C, 150 MPa, 1.5 wt % H_2O and NNO buffer, when the system is H_2O-undersaturated, but the H_2O concentration increases from 1.5 to 3.2 wt % during crystallization (Table S2, Supplementary Materials). Under such circumstances, the plagioclase/clinopyroxene ratio is intermediate (Plg/Cpx = 0.3–1.8) to that experimentally derived at low and high pressure conditions (Figure 4), thus reproducing the bulk rock trachyandesitic compositions of natural products. This finding confirms the differentiation model proposed by [41], where pre-historic trachybasaltic magmas underwent occasional pulses of low-pressure plagioclase fractionation causing the eruption of more evolved trachyandesitic lava flows. Importantly, high-pressure experiments from this study point out that, at H_2O = 2.1–3.2 wt %, the degree of crystallization is generally very high (~40–50 vol %),

so that deep-seated trachybasaltic magmas shift towards phonotephritic compositions never erupted during the entire volcanic activity of Mt. Etna.

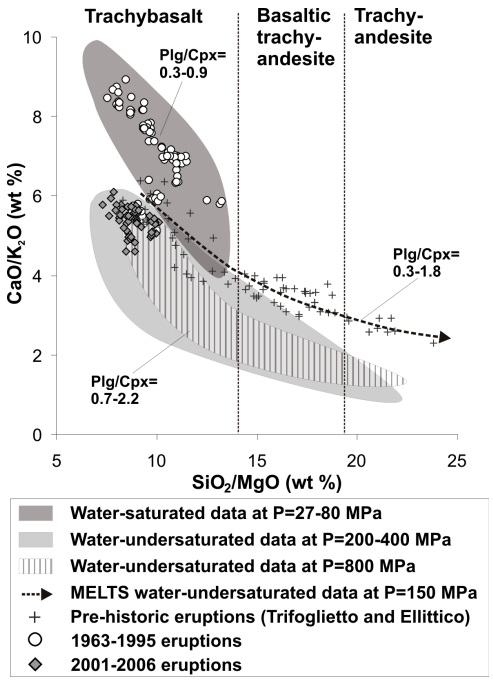

Figure 4. The compositions of pre-historic, 1963–1995, and 2001–2006 lava flows at Mt. Etna (data are from the GEOROC database—http://georoc.mpch-mainz.gwdg.de/georoc/Start.asp) are compared with those experimentally derived at high (P = 800 MPa), moderate (P = 200–400 MPa) and low (P = 27–120 MPa) pressures, as well as MELTS [42] simulations on HE trachybasalt equilibrated at 1000–1160 °C, 150 MPa, 1.5 wt % H_2O and NNO buffer (see dashed line). The Plg/Cpx ratio changes upon the effect of H_2O-saturated and H_2O-undersaturated conditions, controlling the CaO/K_2O ratio of the melt. Plg, plagioclase. Cpx, clinopyroxene.

4.2. H_2O Release upon Magma Ascent during 2001 and 2006 Eruptions

Through the thermodynamically based equation of state proposed by Duan [19], we have estimated the solubility of H_2O and CO_2 in Etnean magmas. One of the advantages of this model consists of its applicability to high pressure (>500 MPa) and high temperature conditions that are not adequately reproduced by previous equations (see [20] for a review). Our calculations referred to 100–800 MPa and 1200 °C using the HE trachybasalt as input composition (Table 1); notably, replicated calculations at 1100–1150 °C with more or less differentiated trachybasalts (MgO = 4–6 wt % as for 2001–2012 Etnean lavas; [12]) provided changes in estimate (6.5%) within the accuracy of the model for the prediction of H_2O (7.2%) and CO_2 (9.7%). Results are plotted in Figure 5a together with the volatile contents derived by melt inclusion data from 2001 and 2006 lava flows [3,14,43]. Generally, the molar fraction of H_2O in the gas phase ranges from 20 to 40 mol % as documented by Collins et al. [3] and, at ~400 MPa, the maximum concentrations of H_2O and CO_2 are 3.5 wt % and 0.3 wt %, respectively (Figure 5a). The amount of volatiles dissolved in the 2001 magma is also higher than that measured for the 2006 eruption. Indeed, the 2001 lava flow was fed by a volatile-rich primitive basalt rising along a closed-system degassing path [14,43], whereas the 2006 eruption involved the slow effusion of a gas-poor magma ponding within the volcanic edifice [3,44]. An important outcome from our calculations is that, at 800 MPa, the solubility of H_2O can be very high, ranging from 6 to 8.5 wt % (Figure 5a). Therefore, trachybasaltic magmas stored at the Moho depth may be source of sustained H_2O supply during upward migration throughout the plumbing system of the volcano.

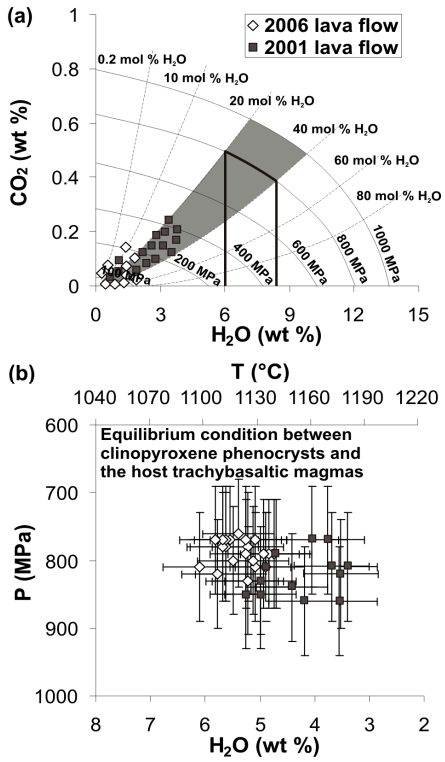

Figure 5. H_2O vs. CO_2 solubility diagram derived through the model of Duan [19] (**a**). Calculations were referred to 100–800 MPa and 1200 °C using the HE trachybasalt as input composition. The volatile contents derived by melt inclusion data from 2001 and 2006 lava flows [3,14,43] are also plotted in figure. P-T-H_2O diagram derived for the stability of clinopyroxene phenocrysts from 2001 and 2006 lava flows (**b**). The saturation pressure (~800 MPa) and temperature (1120–1200 °C and 1080–1150 °C for the 2001 and 2006 clinopyroxenes, respectively) were estimated by Armienti et al. [21]. Our experimental data, indicate that the original amounts of H_2O in equilibrium with 2001 and 2006 magmas were 3–6 and 5.5–7 wt %, respectively. Error bars come from thermometric and hygrometric estimates of Armienti et al. [21].

Using a specific algorithm based on the equilibrium partitioning between mineral and melt, Armienti et al. [21] estimated the near-liquidus temperature of Etnean trachybasaltic magmas at the early stage of clinopyroxene crystallization. At ~800 MPa, the authors found that clinopyroxene saturation occurred at 1120–1200 °C and 1080–1150 °C for the 2001 and 2006 composition, respectively (Figure 5b). Looking at our experimental data, clinopyroxene is in equilibrium with a trachybasaltic magma when the degree of crystallization is $\leq$13 vol % (Table 2), otherwise the melt composition would readily evolve towards either basaltic trachyandesite or phonotephrite as a function of H_2O (Figure 2). The trachybasaltic melts experimentally-derived in this study confirm that the temperatures estimated by Armienti et al. [21] are close to the near-liquidus region of the 2001 and 2006 eruptions. Figure 1 shows that, as the temperature decreases, the near-liquidus surface is controlled by increasing amounts of H_2O. According to this experimental curve, we found that the original H_2O concentrations in equilibrium with 2001 and 2006 magmas were 3–6 wt %. Coherently, these H_2O contents closely match with the hygrometric estimates of 3–6 and 5.5–7 wt % for 2001 and 2006 eruptions, respectively, reported by Armienti et al. [21] (Figure 5b). With respect to the degassed melt inclusions found at the storage level of ~200 MPa (see also [1]), our experimental data provide quantification for the overall release of H_2O (1.5–4 wt %) that could be expected during impulsive ascent of deep-seated trachybasaltic magmas at Mt. Etna [4,45,46]. A migration of volatiles (particularly H_2O) transported as supercritical fluids throughout the Etnean plumbing system is also consistent with the early "volatile-induced differentiation model" proposed by Ferlito and Lanzafame [8] and further reappraised by Ferlito [47] to explain the potassium enrichment observed in post-1971 lava flows and the transition from a

low-density H_2O-melt solution to a high-density melt phase erupted concomitant to a sustained gas flux. Therefore, the huge flux of magmatic gases from depth provides explanation for (1) the low volume of magma erupted in recent years with respect to the great amount of gases measured in the volcanic plume [5,47], (2) the compositions of unusually explosive eruptions fed by primitive, volatile-rich magmas [48], and (3) the textural and compositional variations of plagioclases related to fluid-induced dissolution reactions [9]. In this context, Figure 6 shows that, at 800 MPa and 1070–1090 °C, the basaltic trachyandesitic magma is saturated with clinopyroxene when the amount of H_2O is 5.2–8 wt %. Conversely, at 200–400 MPa and 1050–1070 °C, the H_2O content decreases to 2.5–4 wt %, implying that at least 50% of H_2O is released as a free fluid phase. Both melt inclusion data [3,43] and clinopyroxene-based hygrometric estimates [39,49] confirm that H_2O degassing starts at ~400 MPa, with most of the H_2O loss occurring at P < 100 MPa.

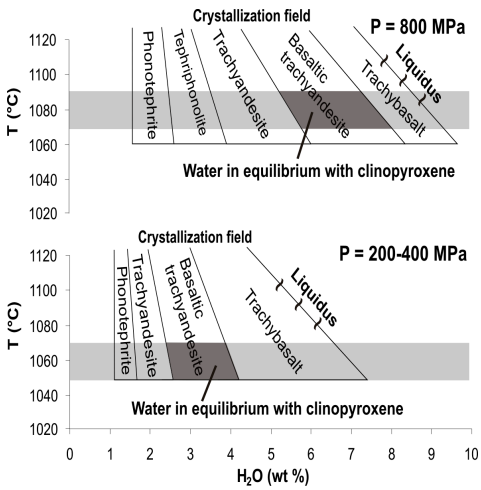

Figure 6. Temperature vs. H_2O diagram derived using data from hydrous crystallization experiments conducted at high (800 MPa from this study) and moderate (200–400 MPa from literature) pressures. Considering the natural P-T constrains of 2011–2013 lava fountains, the amount of H_2O in equilibrium with clinopyroxene phenocrysts has been reconstructed. At 800 MPa and 1070–1090 °C, the basaltic trachyandesitic magma is saturated with clinopyroxene when the amount of H_2O is 5.2–8 wt %. Conversely, at 200–400 MPa and 1050–1070 °C, the H_2O content decreases to 2.5–4 wt %.

5. Conclusions

High-pressure crystallization experiments carried out on a trachybasaltic composition, under H_2O-undersaturated and H_2O-saturated conditions, shed new light on the role of H_2O on the high-pressure crystallization path of magma at Mt. Etna. We found that the crystallization sequence, phase stability, textural and compositional evolution of natural minerals are directly correlated to the transition from H_2O-undersaturated to H_2O-saturated crystallization regimes. Olivine is a late crystallizing phase from H_2O-undersaturated magmas equilibrated at high pressure. In contrast, the clinopyroxene saturation surface is encountered at 800 MPa, when the solubility of H_2O can be very high, ranging from 6 to 8.5 wt %. During upward migration throughout the plumbing system of the volcano, the overall release of H_2O accompanying clinopyroxene crystallization is constrained between 1.5 and 4 wt %. Therefore, the impulsive ascent of deep-seated trachybasaltic magmas may release a great amount of H_2O. Most of the excess of H_2O may contribute to the gas emissions from the summit craters and volcano flanks feeding the persistent gas plume at Mt. Etna. However, high-pressure experiments conducted at H_2O-undersaturated conditions cannot account for the distinctly non-equilibrium processes related to the large gas flux that may control magma compositions and trigger eruptions at Mt. Etna volcano. Therefore, further laboratory investigations on decompression and volatile degassing mechanisms may be of help to elucidate magma dynamics related to intense supply of a gas phase (mostly H_2O) in the uppermost section of the feeding system.

Supplementary Materials: The following are available online at http://www.mdpi.com/2075-163X/8/11/482/s1: Table S1. Natural and experimental compositions of Etnean melts; Table S2. MELTS simulations conducted using the HE trachybasalt as starting composition.

Author Contributions: Conceptualization, C.P., S.M. and M.G.; formal analysis, C.P. and S.P.D.C.; investigation, C.P., S.M., M.G. and S.P.D.C.; data curation, C.P.; S.M. and S.P.D.C.; writing—original draft reparation, C.P., S.M., M.G., S.P.D.C., D.M.P., P.S.; writing—review and editing, C.P., S.M., M.G., S.P.D.C., D.M.P., P.S.; visualization, C.P., S.M., M.G., S.P.D.C., D.M.P., P.S.; funding acquisition, M.G., P.S.

Funding: This research received no external funding.

Acknowledgments: We kindly thank M. Serracino for assistance during electron microprobe analysis. Two anonymous reviewers provided instructive and helpful reviews that greatly contributed to the quality of this work.

Conflicts of Interest: The authors declare no conflicts of interest.

References

1. Corsaro, R.A.; Di Renzo, V.; Distefano, S.; Miraglia, L.; Civetta, L. Relationship between petrologic processes in the plumbing system of Mt. Etna and the dynamics of the eastern flank from 1995 to 2005. *J. Volcanol. Geotherm. Res.* **2013**, *251*, 75–89. [CrossRef]
2. Kamenetsky, V.S.; Pompilio, M.; Métrich, N.; Sobolev, A.V.; Kuzmin, D.V.; Thomas, R. Arrival of extremely volatile-rich high-Mg magmas changes explosivity of Mount Etna. *Geology* **2007**, *35*, 255–258. [CrossRef]
3. Collins, S.J.; Pyle, D.M.; Maclennan, J. Melt inclusions track pre-eruption storage and dehydratation of magmas at Etna. *Geology* **2009**, *6*, 571–574. [CrossRef]
4. Ferlito, C.; Viccaro, M.; Cristofolini, R. Volatile-induced magma differentiation in the plumbing system of Mt. Etna volcano (Italy): Evidence from glass in tephra of the 2001 eruption. *Bull. Volcanol.* **2008**, *70*, 455–473. [CrossRef]
5. Ferlito, C.; Coltorti, M.; Lanzafame, G.; Giacomoni, P.P. The volatile flushing triggers eruptions at open conduit volcanoes: Evidence from Mount Etna volcano (Italy). *Lithos* **2014**, *184–187*, 447–455. [CrossRef]
6. Bozzano, F.; Gaeta, M.; Lenti, L.; Martino, S.; Paciello, A.; Palladino, D.M.; Sottili, G. Modeling the effects of eruptive and seismic activities on flank instability at Mount Etna, Italy. *J. Geophys. Res. Solid Earth* **2013**, *118*, 5252–5273. [CrossRef]
7. Mollo, S.; Scarlato, P.; Lanzafame, G.; Ferlito, C. Deciphering lava flow post-eruption differentiation processes by means of geochemical and isotopic variations: A case study from Mt. Etna volcano. *Lithos* **2013**, *162–163*, 115–127. [CrossRef]
8. Ferlito, C.; Lanzafame, G. The role of supercritical fluids in the potassium enrichment of magmas at Mount Etna volcano (Italy). *Lithos* **2010**, *119*, 642–650. [CrossRef]
9. Giacomoni, P.P.; Ferlito, C.; Coltorti, M.; Bonadiman, C.; Lanzafame, G. Plagioclase as Archive of Magma Ascent Dynamics on "Open Conduit" Volcanoes: The 2001–2006 Eruptive Period at Mount Etna. *Earth Sci. Rev.* **2014**, *138*, 371–393. [CrossRef]
10. Armienti, P.; Tonarini, S.; Innocenti, F.; D'Orazio, M. Mount Etna pyroxene as tracer of petrogenetic processes and dynamics of the feeding system. In *Cenozoic Volcanism in the Mediterranean*; Beccaluva, L., Bianchini, G., Wilson, M., Eds.; Geological Society of America Special Papers: Boulder, CO, USA, 2007; Volume 418, pp. 265–276.
11. Lanzafame, G.; Mollo, S.; Iezzi, G.; Ferlito, C.; Ventura, G. Unraveling the solidification path of a *pahoehoe* "cicirara" lava from Mount Etna volcano. *Bull. Volcanol.* **2013**, *75*, 703. [CrossRef]
12. Mollo, S.; Giacomoni, P.P.; Coltorti, M.; Ferlito, C.; Iezzi, G.; Scarlato, P. Reconstruction of magmatic variables governing recent Etnean eruptions: Constraints from mineral chemistry and P-T-fO_2-H_2O modelling. *Lithos* **2015**, *212–215*, 311–320. [CrossRef]
13. Mollo, S.; Giacomoni, P.P.; Andronico, D.; Scarlato, P. Clinopyroxene and titanomagnetite cation redistributions at Mt. Etna volcano (Sicily, Italy): Footprints of the final solidification history of lava fountains and lava flows. *Chem. Geol.* **2015**, *406*, 45–54. [CrossRef]
14. Métrich, N.; Allard, P.; Spilliaert, N.; Andronico, D.; Burton, M. 2001 flank eruption of the alkali- and volatile-rich primitive basalt responsible for Mount Etna's evolution in the last three decades. *Earth Planet. Sci. Lett.* **2004**, *228*, 1–17. [CrossRef]

15. Dolfi, D.; Trigila, R. Clinopyroxene solid solutions and water in magmas: Results in the system phonolitic tephrite-H_2O. *Mineral. Mag.* **1983**, *47*, 347–351. [CrossRef]
16. Metrich, N.; Rutherford, M.J. Low pressure crystallization paths of H_2O-saturated basaltic-hawaitic melts from Mt Etna: Implications for open-system degassing of basaltic volcanoes. *Geochim. Cosmochim. Acta* **1998**, *62*, 1195–1205. [CrossRef]
17. Vetere, F.; Mollo, S.; Giacomoni, P.P.; Iezzi, G.; Coltorti, M.; Ferlito, C.; Holtz, F.; Perugini, D.; Scarlato, P. Experimental constraints on the origin of pahoehoe "cicirara" lavas at Mt. Etna Volcano (Sicily, Italy). *Bull. Volcanol.* **2015**, *77*, 44. [CrossRef]
18. Hirn, A.; Nicolich, R.; Gallart, J.; Laigle, M.; Cernobori, L.; ETNASEIS Scientific Group. Roots of Etna volcano in faults of great earthquakes. *Earth Planet. Sci. Lett.* **1997**, *148*, 171–191. [CrossRef]
19. Duan, X. A general model for predicting the solubility behavior of H_2O-CO_2 fluids in silicate melts over a wide range of pressure, temperature and compositions. *Geochim. Cosmochim. Acta* **2014**, *125*, 582–609. [CrossRef]
20. Mitchell, A.L.; Gaetani, G.A.; O'Leary, J.A.; Hairi, E.H. H_2O solubility in basalt at upper mantle conditions. *Contrib. Mineral. Petrol.* **2017**, *172*, 85. [CrossRef]
21. Armienti, P.; Perinelli, C.; Putirka, K.D. A new model to estimate deep-level magma ascent rates, with applications to Mt. Etna (Sicily, Italy). *J. Petrol.* **2013**, *54*, 795–813. [CrossRef]
22. Armienti, P.; Clocchiatti, R.; D'Orazio, M.; Innocenti, F.; Petrini, R.; Pompilio, M.; Tonarini, S.; Villari, L. The long-standing 1991–1993 Mount Etna eruption: Petrography and geochemistry of lavas. *Acta Vulcanol.* **1994**, *4*, 15–28.
23. Andronico, D.; Corsaro, R.A. Lava fountains during the episodic eruption of South–East Crater (Mt. Etna), 2000: Insights into magma-gas dynamics within the shallow volcano plumbing system. *Bull. Volcanol.* **2011**, *73*, 1165–1178. [CrossRef]
24. Viccaro, M.; Giacomoni, P.P.; Ferlito, C.; Cristofolini, R. Dynamics of magma supply at Mt. Etna volcano (Southern Italy) as revealed by textural and compositional features of plagioclase phenocrysts. *Lithos* **2010**, *116*, 77–91. [CrossRef]
25. Devine, J.D.; Gardner, J.E.; Brack, H.P.; Laynet, G.D.; Rutherford, M.J. Comparison of microanalytical methods for estimating H_2O contents of silicic volcanic glasses. *Am. Mineral.* **1995**, *80*, 319–328. [CrossRef]
26. Corsaro, R.A.; Pompilio, M. Dynamics of magmas at Mount Etna. In *Mt. Etna Volcano Laboratory*; Bonaccorso, A., Calvari, S., Coltelli, M., Del Negro, C., Falsaperla, S., Eds.; AGU Geophysical Monograph Series: Washington, DC, USA, 2004; Volume 143, pp. 91–110.
27. Kress, V.G.; Charmichael, I.S.E. The compressibility of silicate liquids containing Fe_2O_3 and the effect of composition, temperature, oxygen fugacity and pressure on their redox state. *Contrib. Mineral. Petrol.* **1991**, *108*, 82–92. [CrossRef]
28. Toplis, M.J. The thermodynamics of iron and magnesium partitioning between olivine and liquid: Criteria for assessing and predicting equilibrium in natural and experimental systems. *Contrib. Mineral. Petrol.* **2005**, *149*, 22–39. [CrossRef]
29. Conte, A.M.; Dolfi, D.; Gaeta, M.; Misiti, V.; Mollo, S.; Perinelli, C. Experimental constraints on evolution of leucite-basanite magma at 1 and 10^{-4} GPa: Implications for parental compositions of Roman high-potassium magmas. *Eur. J. Mineral.* **2009**, *21*, 763–782. [CrossRef]
30. Weaver, S.L.; Wallace, P.J.; Johnston, A.D. Experimental constraints on the origins of primitive potassic lavas from the Trans-Mexican Volcanic Belt. *Contrib. Mineral. Petrol.* **2013**, *166*, 825–843. [CrossRef]
31. Stormer, J.C.; Nicholls, J. XLFRAC: A program for the interactive testing of magmatic differentiation models. *Comput. Geosci.* **1978**, *4*, 143–159. [CrossRef]
32. Lange, R.A.; Carmichael, I.S.E. Densities of Na_2O-K_2O-CaO-MgO-FeO-Fe_2O_3-Al_2O_3-TiO_2-SiO_2 liquids: New measurements and derived partial molar properties. *Geochim. Cosmochim. Acta* **1987**, *51*, 2931–2946. [CrossRef]
33. Mollo, S.; Del Gaudio, P.; Ventura, G.; Iezzi, G.; Scarlato, P. Dependence of clinopyroxene composition on cooling rate in basaltic magmas: Implications for thermobarometry. *Lithos* **2010**, *118*, 302–312. [CrossRef]
34. Frey, H.M.; Lange, R.A. Phenocryst complexity in andesites and dacites from the Tequila volcanic field, Mexico: Resolving the effects of degassing vs. magma mixing. *Contrib. Mineral. Petrol.* **2011**, *162*, 415–445. [CrossRef]

35. Putirka, K.D. Thermometers and barometers for volcanic systems. *Rev. Mineral. Geochem.* **2008**, *69*, 61–120. [CrossRef]
36. Putirka, K.D.; Mikaelian, H.; Ryerson, F.; Shaw, H. New clinopyroxene-liquid thermobarometers for maric, evolved, and volatile-bearing lava compositions, with applications to lavas from Tibet and the Snake River Plain, Idaho. *Am. Mineral.* **2003**, *88*, 1542–1554. [CrossRef]
37. Mollo, S.; Putirka, K.; Iezzi, G.; Scarlato, P. The control of cooling rate on titanomagnetite composition: Implications for a geospeedometry model applicable to alkaline rocks from Mt. Etna volcano. *Contrib. Mineral. Petrol.* **2013**, *165*, 457–475. [CrossRef]
38. Mollo, S.; Masotta, M. Optimizing pre-eruptive temperature estimates in thermally and chemically zoned magma chambers. *Chem. Geol.* **2014**, *368*, 97–103. [CrossRef]
39. Mollo, S.; Blundy, J.; Scarlato, P.; De Cristofaro, S.P.; Tecchiato, V.; Di Stefano, F.; Vetere, F.; Holtz, F.; Bachmann, O. An integrated *P*-*T*-H_2O-lattice strain model to quantify the role of clinopyroxene fractionation on REE+Y and HFSE patterns of mafic alkaline magmas: Application to eruptions at Mt. Etna. *Earth Sci. Rev.* **2018**, *185*, 32–56. [CrossRef]
40. Di Carlo, I.; Pichavant, M.; Rotolo, S.G.; Scaillet, B. Experimental Crystallization of a High-K Arc Basalt: The Golden Pumice, Stromboli Volcano (Italy). *J. Petrol.* **2006**, *47*, 1317–1343. [CrossRef]
41. Tanguy, J.C.; Condomines, M.; Kieffer, G. Evolution of the Mount Etna magma: Constraints on the present feeding system and eruptive mechanism. *J. Volcanol. Geotherm. Res.* **1997**, *75*, 221–250. [CrossRef]
42. Ghiorso, M.S.; Sack, R.O. Chemical mass-transfer in magmatic processes IV. A revised and internally consistent thermodynamic model for the interpolation and extrapolation of liquidus-solid equilibria in magmatic systems at elevated temperatures and pressures. *Contrib. Mineral. Petrol.* **1995**, *119*, 197–212. [CrossRef]
43. Spilliaert, N.; Allard, P.; Metrich, N.; Sobolev, A.V. Melt inclusion record of the conditions of ascent, degassing, and extrusion of volatile-rich alkali basalt feeding the powerful 2002 flank eruption of Mount Etna (Italy). *J. Geophys. Res.* **2006**, *111*, B04203. [CrossRef]
44. Aiuppa, A.; Federico, C.; Giudice, G.; Gurrieri, S.; Liuzzo, M.; Shinohara, H.; Favara, R.; Valenza, M. Rates of carbon dioxide plume degassing from Mount Etna volcano. *J. Geophys. Res.* **2006**, *111*, B09207. [CrossRef]
45. Le Cloarec, M.F.; Pennisi, M. Radionuclides and sulfur content in Mount Etna plume in 1983–1995: New constraints on the magma feeding system. *J. Volcanol. Geotherm. Res.* **2001**, *108*, 141–155. [CrossRef]
46. Allard, P.; Behncke, B.; D'Amico, S.; Neri, M.; Gambino, S. Mount Etna 1993–2005: Anatomy of an evolving eruptive cycle. *Earth Sci. Rev.* **2006**, *78*, 85–114. [CrossRef]
47. Ferlito, C. Mount Etna volcano (Italy). Just a giant hot spring! *Earth Sci. Rev.* **2018**, *177*, 14–23. [CrossRef]
48. Ferlito, C.; Viccaro, M.; Nicotra, E.; Cristofolini, R. Regimes of magma recharge and their control on the eruptive behaviour during the period 2001–2005 at Mt. Etna volcano. *Bull. Volcanol.* **2012**, *74*, 533–543. [CrossRef]
49. Perinelli, C.; Mollo, S.; Gaeta, M.; De Cristofaro, S.P.; Palladino, D.M.; Armienti, P.; Scarlato, P.; Putirka, K.D. An improved clinopyroxene-based hygrometer for Etnean magmas and implications for eruption triggering mechanisms. *Am. Mineral.* **2016**, *101*, 2774–2777. [CrossRef]